Rare Met. (2023) 42(3):797–805
https://doi.org/10.1007/s12598-022-02179-8

RARE METALS

LETTER

2D Co metal-organic framework nanosheet as an oxidase-like nanozyme for sensitive biomolecule monitoring

Jia-Wei Guo, Zhong-Wei Yang, Xiu-Li Liu, Li-Wei Zhang, Wei-Bo Guo*, Jian Zhang, Long-Hua Ding*

Received: 25 June 2022 / Revised: 31 July 2022 / Accepted: 12 August 2022 / Published online: 13 December 2022

Nanozyme-based biomolecules sensitive and quantitative detection is an attractive strategy due to their high chemical, thermal stability and reactive activity. Here, we have synthesized a significant number of two-dimensional (2D) cobalt-metal-organic framework (Co-MOF) nanosheets with oxidase (OXD)-like activity using a facile solvothermal method in one pot for biomolecule monitoring. The synthesized Co-MOF nanosheets exhibit strong stability, higher specific surface area and more active sites due to their MOF structure. Such Co-MOF nanosheets with excellent OXD-like activity show adequate analytical performance in the quantitative determination of dopamine (DA) and glutathione (GSH) with a wider dynamic sensing range and lower detection limits (DA and GSH: 0.24 and 0.067 μmol·L^{-1}, 3σ/slope, where σ is standard deviation of the blank). This work extends the application of 2D-MOF structures in bioassays and brings new insights into the application of OXD-like nanozymes in bioassays.

Natural enzymes play significant roles in various biochemical processes and have potential application prospects in biotechnology and environmental remediation [1]. However, their relatively low stability, high cost and difficulties in storage restricted their practical applications [2–5]. Aiming to overcome these drawbacks, researchers have been developing nanomaterials with enzymatic activity (nanozymes), which are highly stable, low cost, scale-up, easy preparation and catalytically efficient [6]. These merits make nanozymes an excellent replacement for natural enzymes [7–9].

Since Yan et al. discovered that Fe_3O_4 has intrinsic peroxidase (POD)-like property in 2007, plenty of nanomaterials with enzyme-mimic activity have been designed and synthesized [10]. At present, most of the reported nanozymes show POD activity and H_2O_2 is needed in the catalytic oxidation process [11, 12]. Oxidases (OXD) can catalyze the oxidation of substances in the presence of oxygen (O_2) instead of H_2O_2, which makes OXD more convenient and safer than peroxidase in biosensor construction, anti-inflammatory and sterilization [13, 14]. However, only a few kinds of nanomaterials (such as CeO_2, Mn_xO_y and AuNPs) exhibit oxidase-mimic properties.

Metal-organic frameworks (MOFs) consist of metal ions and organic ligands, which are a class of hybrid inorganic-organic crystalline porous materials [15–17]. Furthermore, MOFs can be synthesized briefly by solvothermal, microwave-assisted, ultrasonic, and electrochemical methods [18–21]. They have attracted much interest due to their prominent features, such as high specific surface area, excellent stability, flexible nanoscale porosity and abundant spatial structure, which make them have been applied

Wei-Jia Guo and Zhong-Wei Yang have contributed equally to this work.

Supplementary Information The online version contains supplementary material available at https://doi.org/10.1007/s12598-022-02179-8.

J.-W. Guo, Z.-W. Yang, X.-L. Liu, L.-W. Zhang, L.-H. Ding*
Institute for Advanced Interdisciplinary Research, School of Chemistry and Chemical Engineering, University of Jinan, Jinan 250022, China
e-mail: bio_dinglh@ujn.edu.cn

W.-B. Guo*
School of Chemistry and Chemical Engineering, Linyi University, Linyi 276005, China
e-mail: weiboguo@126.com

J. Zhang
Department of Biology and Biological Engineering, Chalmers University of Technology, 41296 Göteborg, Sweden

in gas separation, energy storage, catalysis, sensors, biomedical imaging, etc. [22–24]. In addition, MOFs-based materials are also explored as nanozymes. However, there are often some modified MOFs and some MOF derivatives that exhibit OXD-like activity, while pristine MOFs show POD-like properties. So far, only a few pristine MOFs with OXD-like activity have been reported [25]. Tan et al. synthesized mixed-valence state cerium-MOF (MVC-MOF) with OXD-like activity [26]. Indeed, the development of pristine MOFs with OXD-mimic activity is still in its infancy and it is a challenging object [27].

Herein, we exploit a facile solvothermal method for the one-pot synthesis of 2D Co-MOF with a large specific surface area and high stability (Scheme 1). The as-prepared Co-MOF nanosheets possess OXD-like activity. Owing to the MOF structure, the specific surface area of the composite structure can reach 90.7 $m^2 \cdot g^{-1}$, which can expose more catalytically active sites. Furthermore, the Co-MOF nanosheets exhibit strong stability. Based on these results, a simple, sensitive and selective colorimetric method was established for the quantitative detection of DA and GSH. The linearity between the analyte concentration and absorption ranged from 0 to 12 $\mu mol \cdot L^{-1}$ for GSH and 0 to 40 $\mu mol \cdot L^{-1}$ for DA with a detection limit of 0.24 and 0.067 $\mu mol \cdot L^{-1}$ for GSH and DA.

The Co-MOF was synthesized through the hydrothermal method as shown in Scheme 1. Firstly, the morphology of the as-prepared Co-MOF was observed through scanning electron microscopy (SEM). As shown in Fig. 1a, the Co-MOF consists of a wealth of 3D flower-like microstructures (diameter of about 5 μm) composed of 2D nanosheets. The diameter of the nanosheet is 0.5–1 μm (Fig. 1b). The results observed from the transmission electron microscopy (TEM) image (Fig. 1c) were consistent with those from SEM images. In addition, from the high-resolution TEM (HRTEM) image, the typical interlaminar spacing of 0.22 nm could be observed (Fig. 1d), which belongs to the typical Co-MOF structure. Furthermore, energy-dispersive spectrometer (EDS) elemental mapping of Co-MOF (Fig. 1e) confirmed the existence of Co, N, O and C. Moreover, the elements are evenly distributed within the nanostructure.

X-ray diffraction (XRD) analysis was employed to characterize the crystal phase of Co-MOF. The diffraction peak is located at about 10.5° belonging to 2-MI of Co-MOF (Fig. 2a) [28]. Subsequently, the light absorption ability of Co-MOF was investigated by ultraviolet-visible (UV-Vis) diffuse reflection spectrum (DRS; Fig. S1). Co-MOF nanosheets show a light absorption edge at 650 nm, which is located in the visible region. And Co-MOF

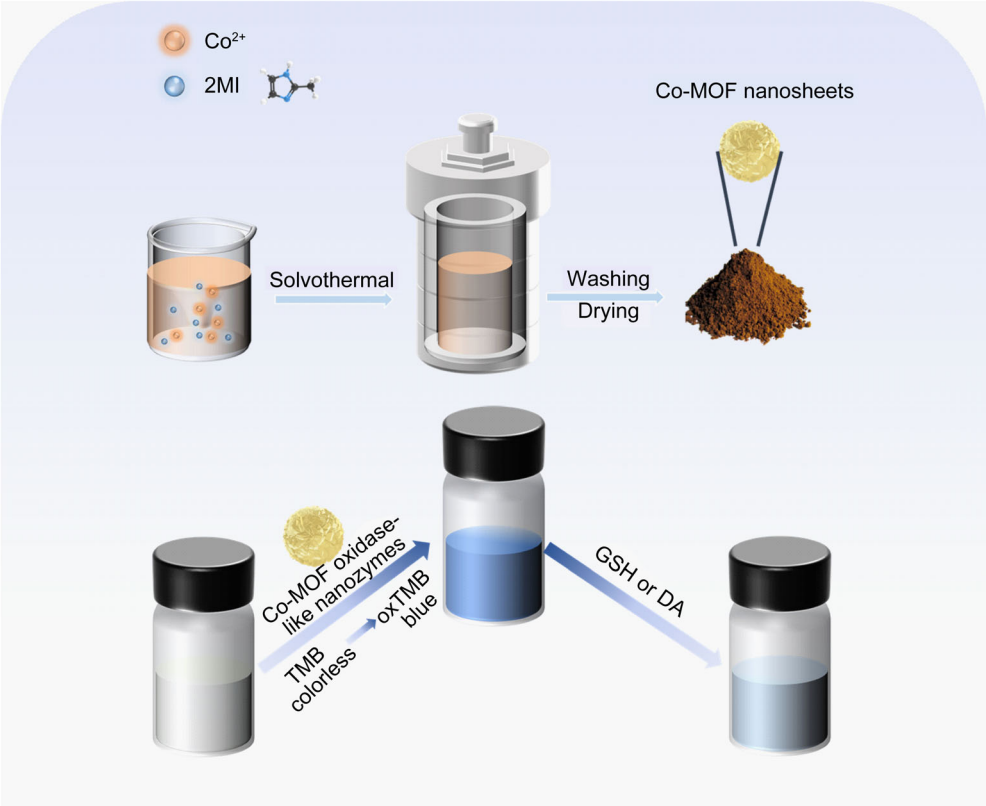

Scheme 1 Synthesis of Co-MOF and detection mechanism of GSH and DA

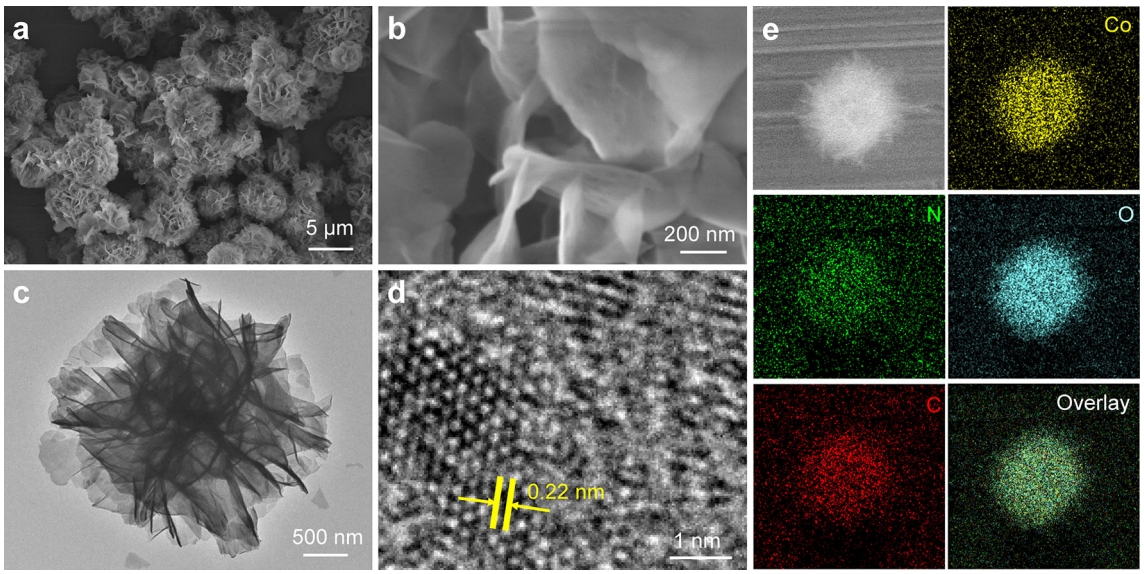

Fig. 1 **a**, **b** SEM, **c** TEM, and **d** HRTEM images of Co-MOF; **e** EDS elemental maps of Co-MOF

nanosheets also absorb at 1205 nm in the NIR-II region. The properties of the Co-MOF structure were further confirmed by Raman spectra, which are based on the sensitivity of molecular vibrations and rotations. As shown in Fig. S2, the peaks of Co-MOF at 473 and 678.1 cm^{-1} correspond well to the C=N–C vibrations and belong to the bending vibrational peak of the imidazole ring [29, 30]. The peak located at 513.4 cm^{-1} is attributed to the stretching of the Co–O bond. Fourier-transform infrared spectroscopy (FTIR) spectrum was obtained to explore the molecular structure and chemical composition of Co-MOF. A stretching vibration of the C–H bond at 2922 and 2852 cm^{-1} could be observed in Fig. 2b, while 3439 cm^{-1} corresponds to the hydroxyl group (–OH) on the surface of

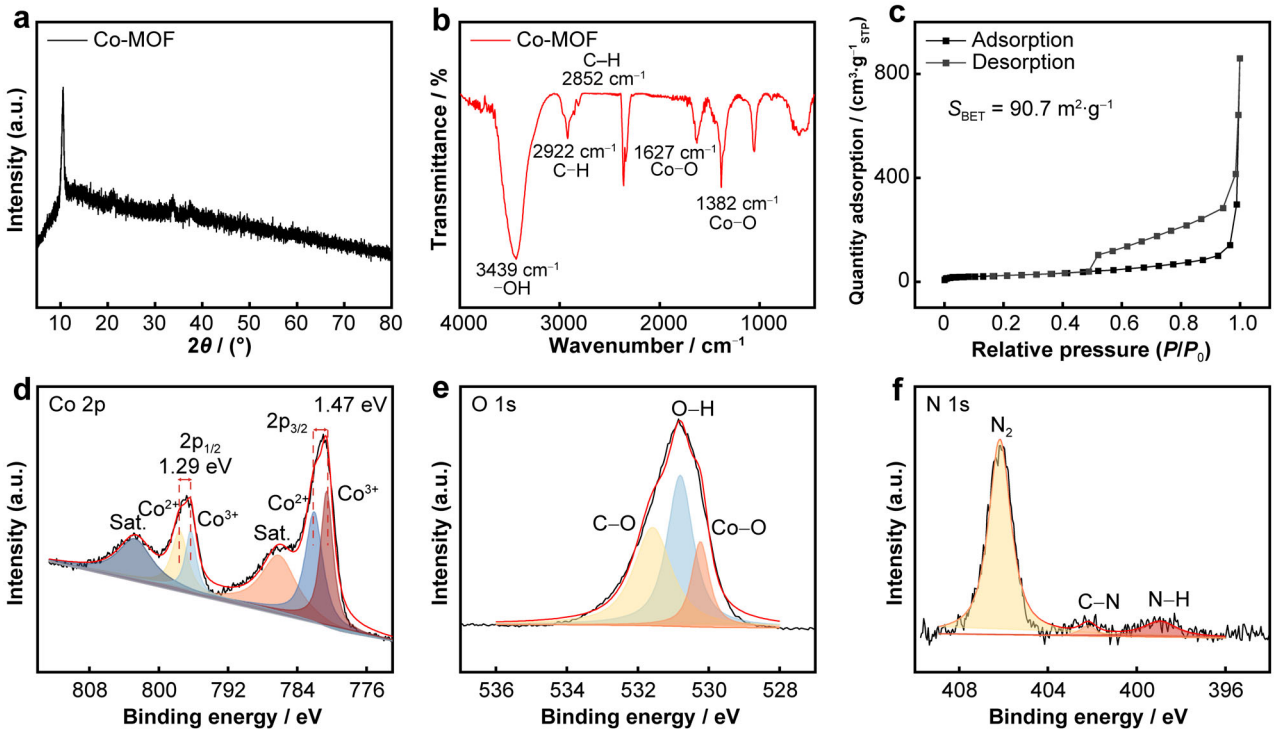

Fig. 2 **a** XRD pattern, **b** FTIR spectrum and **c** N_2 adsorption–desorption isotherms of Co-MOF; high-resolution XPS spectra of **d** Co 2p, **e** O 1s and **f** N 1s

Co-MOF. The peaks located at 1627 and 1382 cm^{-1} are attributed to the Co–O bond in Co-MOF [31]. The specific surface area of Brunauer–Emmett–Teller (BET) of Co-MOF is measured to be 90.7 $m^2 \cdot g^{-1}$ with a most countable pore size of 4.08 nm (Figs. 2c, S3), which is beneficial to the adsorption of detected substances.

The chemical composition and chemical valence were analyzed by X-ray photoelectron spectroscopy (XPS). The full XPS spectrum shown in Fig. S4a indicates the presence of Co, C, N and O in Co-MOF. Considering the two spin–orbit double-peak characteristics of Co^{2+} and Co^{3+} and the two shaky satellites (identified as "Sat."), the Co 2p spectrum (Fig. 2d) can be deconvoluted. For the Co-MOF sample, the peaks at 780.56, 796.28 eV and 782.03, 797.57 eV for the $2p_{3/2}$ and $2p_{1/2}$ orbitals are attributed to Co^{3+} and Co^{2+}, respectively. In addition, it could also be seen two wobbly satellites at 786.11 and 802.73 eV. The Co $2p_{3/2}$ orbit of Co-MOF has a potential barrier of 1.47 eV between + 2 and + 3, while the $2p_{1/2}$ orbit has a potential barrier of 1.29 eV between + 2 and + 3 [32, 33]. Moreover, the characteristic peaks in the O 1s spectrum of Co-MOF at 530.23, 530.8 and 531.58 eV are attributed to Co–O, O–H and C–O bonds, respectively (Fig. 2e). The peaks at 398.94, 402.18 and 406.17 eV in the N 1s spectrum (Fig. 2f) belong to the N–H, C–N and N_2 of Co-MOF. Feature peaks of C 1s belonging to Co-MOF located at 284.13, 284.81, 285.9 and 288.42 eV correspond to C–C, C=C, C–N and C=O bonds, respectively (Fig. S4b).

To evaluate the OXD-like activity of Co-MOF, TMB was used as a substrate because the color change was evident after TMB oxidation and the oxidation product oxTMB had a characteristic absorbance at 652 nm. For comparison, nickel MOF (Ni-MOF) was also synthesized in the same method (shown in Supporting Information). Ni-MOF possessed similar morphologies and BET-specific surface area (88.8 $m^2 \cdot g^{-1}$) and pore size (3.95 nm) (Figs. S5, S6) to Co-MOF. It could be seen in Fig. 3a that the air-saturated solution containing TMB turned blue and showed an absorption peak at 652 nm in the presence of Co-MOF, which was much higher than that of Ni-MOF. Similarly, OPD and ABTS were oxidized to organed and darkgreen substances with characteristic absorption peak at 552 and 418 nm by Co-MOF, respectively, along with characteristic absorption peaks at 452 and 418 nm (Fig. 3b, c). Similarly, the Co-MOF also produces a much higher absorption peak than Ni-MOF. The OXD-like activity of Co-MOF fluctuates with pH and has the highest activity at pH 3.6 (Fig. 3d). In addition, it also shows excellent activity over a wide temperature range with the best activity at 37 °C (Fig. 3e), which is better than natural enzymes.

In principle, OXD-like MOF nanozymes catalyze the dissociation of O_2 into oxygen adsorbed atoms. To check whether O_2 is a substrate for the Co-MOF, the effect of O_2 was tested. Briefly, we added or removed dissolved O_2 from Co-MOF and TMB solutions by air or nitrogen (N_2) purging (30 min) firstly and then monitored the absorption of oxTMB after mixing for 10 min [34]. It could be observed that the absorbance of TMB in the presence of air blowing significantly increased, while in the absence of O_2 (in the presence of N_2), the absorbance of oxTMB decreased (Figs. 3f, S7), indicating a significant inhibition of ROS production after O_2 removal. Overall, these results suggest that Co-MOF was an OXD-like nanozyme.

To further verify the OXD-like activity of Co-MOF, we chose ascorbic acid (AA) as an antioxidant, which shows a strong absorption at 266 nm and disappears after being oxidized [35]. After co-incubation with Co-MOF for 12 h, a dramatic decrease in the absorbance of AA at 266 nm could be observed (Figs. 4a, S8a). It indicates that ROS can be produced by Co-MOF without any external stimulation and would vary with the concentration of Co-MOF increasing (Figs. 4b, S8b). As we all know, singlet oxygen ($^1O_2$) and hydroxyl radicals (·OH) are extremely highly reactive [36], which are the ROS substances generated by most of the nanozymes.

To further validate the source of OXD-like activity of Co-MOF, we used Co-MOF as our representative for ROS generation through probes. 9,10-anthracenediyl-bis (methylene) dimalonic acid (ABDA) is a fluorescent molecule, which could become non-fluorescent after being captured by $^1O_2$. We observed that after co-incubation of Co-MOF (60 $\mu g \cdot mL^{-1}$) with ABDA for 3 h, the relative fluorescence of ABDA decreased by ~ 75.7% (Figs. 4c, S9a) and that this ability was dose-dependent (Figs. 4d, S9b, S9c), implying that Co-MOF produces $^1O_2$-like ROS species. To exclude the possibility that the observed fluorescence reduction of ABDA is due to accidental bleaching of ABDA, singlet oxygen sensor green (SOSG) was also used as a probe for monitoring $^1O_2$, which is weakly blue fluorescent and changes to bright green fluorescence after $^1O_2$ capture [37]. The same bright green fluorescence enhancement of SOSG was observed after co-incubation of SOSG with Co-MOF for 3 h (Figs. 4e, S10). In conclusion, these observations suggested that the ROS generated by Co-MOF should be $^1O_2$ in chemical reactivity. Significantly, Co-MOF does not produce ROS with chemical reactivity similar to ·OH because Co-MOF fails to affect the fluorescence of terephthalic acid (PTA) (Figs. 4f, S11), which is non-fluorescent and can become brightly fluorescent (λ_{em} = 430 nm, where λ_{em} is emission wavelength) upon the capture of ·OH [38]. In conclusion, these results suggest that Co-MOF generates ROS similar to $^1O_2$ in terms of chemical reactivity instead of ·OH.

Bio-thiols, such as glutathione (GSH), play an active role in antioxidant processes which are also biomarkers for

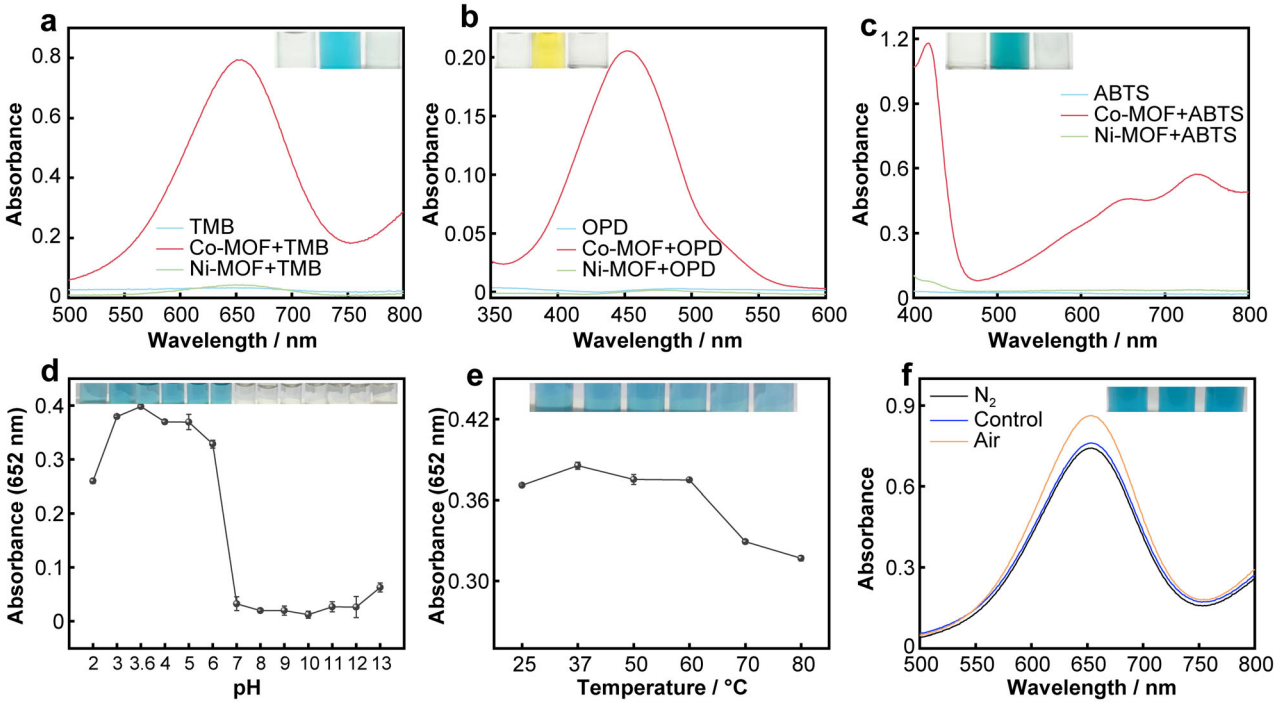

Fig. 3 OXD-like activity of Co-MOF: **a** UV–Vis absorption spectra of TMB with or without Co-MOF or Ni-MOF in air-saturated buffer (inset: digital photos from left to right being TMB, Co-MOF + TMB, and Ni-MOF + TMB solutions after mixing for 10 min); UV–Vis absorption spectra when substrates were replaced with **b** OPD or **c** ABTS with other conditions same as TMB; absorbance at 652 nm in the presence of Co-MOF at different **d** pH values and **e** temperatures; **f** UV–Vis absorption spectra of TMB in the presence of Co-MOF in N_2, air-saturated buffer and air purge (inset: digital photos from left to right being N_2, air-saturated buffer and air purge pre-purged for 30 min and then mixed for 10 min)

various diseases (liver damage, Alzheimer's disease and cancer) [39–43]. Given the excellent inherent OXD-like activity of Co-MOF, a GSH and DA colorimetric detection system could be established. Co-MOF catalyzes the generation of $^1O_2$ from O_2, which could oxidize TMB to oxTMB. After GSH addition, the blue color of oxTMB changes light gradually and the absorption at 652 nm decreases (Fig. 5a), indicating that GSH can inhibit the oxidation of TMB. Furthermore, the inhibited degree is related to GSH concentration. Figure 5b shows the linear curve between absorption of oxTMB and the concentration of GSH from 0 to 12 μmol·L^{-1}. The regression equation is $y = -0.03629x + 0.51058$ ($R^2 = 0.986$) and the limit of detection is 0.067 μmol·L^{-1} (3σ/slope), indicating a high sensitivity toward GSH. Next, we compared the analytical performance of the proposed method with previously reported sensors with different detection methods for GSH detection (Table S1). It was found that our proposed sensor showed a wider linear detection range and lower LOD value compared to most of the reported sensors.

Similarly, dopamine (DA, 3, 4-dihydroxyphenylalanine) is a key neurotransmitter in the hypothalamus and pituitary glands, which plays an essential role in the central nervous, renal, hormonal and cardiovascular systems [44, 45]. DA concentrations have been connected with neurological and physiological disorders such as schizophrenia, Parkinson's disease, HIV infection and addictive behaviors [46]. We also use the same approach to develop a simple and sensitive colorimetric method for DA determination. Under optimal conditions, the sensitivity of the sensor system was investigated by introducing different concentrations of DA. With DA concentration increasing, the absorption signals at 652 nm gradually diminish. When the concentration of DA reaches 40 μmol·L^{-1}, the absorption value is stable (Fig. 5c). As shown in Fig. 5d, there is a good linear relationship between absorbance and DA concentration from 0 to 40 μmol·L^{-1} with the regression equation $y = -0.01029x + 0.55609$ ($R^2 = 0.987$). The detection limit is 0.24 μmol·L^{-1} (3σ/slope). Furthermore, the color changes of the corresponding samples containing different amounts of DA can be clearly distinguished by visual inspection. Thus, the Co-MOF-based sensor platform provides a simple method for the visual detection of DA. As summarized in Table S2, the colorimetric sensor based on Co-MOF nanosheets oxidase-like nanozyme exhibits relatively lower LOD and wider linear detection range than most of other reported sensors.

The specificity of the proposed method was investigated by adding some interferences, such as bovine serum albumin, histidine, L-arginine, L-leucine, L-threonine and

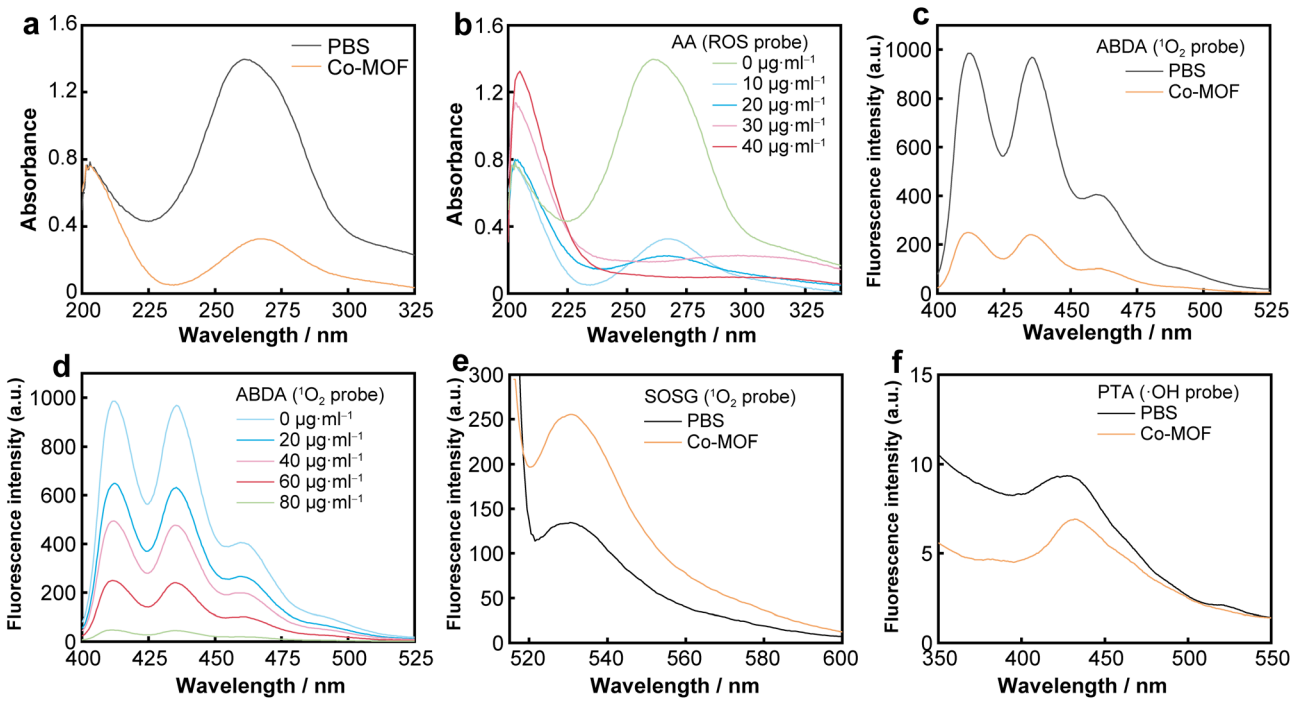

Fig. 4 **a** UV–Vis absorption spectra of AA treated with a Co-MOF (10 μg·ml^{-1} in PBS) or PBS; **b** UV–Vis absorption spectra of AA treated with Co-MOF at different concentrations; **c** fluorescent emission spectra of ABDA after 3-h treatment with Co-MOF (60 μg·ml^{-1}) in PBS, with that of ABDA, treated similarly but with PBS included as a control; **d** fluorescent emission spectra of ABDA after 3-h treatment with Co-MOF at different concentrations; **e** fluorescent emission spectra of SOSG treated with Co-MOF (50 μg·ml^{-1}, for 3 h), with that of SOSG-treated similarly but with PBS included as a control; **f** fluorescent emission spectra of PTA treated with Co-MOF (50 μg·ml^{-1}, for 3 h), with that of PTA-treated similarly but with PBS included as a control

glycine, to the sensing system. As depicted in Fig. 5e, the color of all control samples remains dark blue except for GSH and DA, indicating high selectivity of the as-constructed sensing platform. The results show that the prepared assay system is resistant to the interference of other amino acids. These phenomena validate the good specificity of the Co-MOF. In addition, the stability of Co-MOF was assessed by measuring the absorption of oxTMB produced by a reaction between TMB and Co-MOF at different time. As shown in Fig. 5f, the catalytic activity almost remains unchanged for a long period. Furthermore, XPS and XRD spectra of Co-MOF were also tested after the reaction with GSH and DA. From the full spectrum of Fig. S12a, it could be seen that Co-MOF + GSH has sulfur production after the reaction, which may be originated from the sulfhydryl group (−SH) with GSH. These same Co 2p peaks of Co-MOF + DA and Co-MOF + GSH also shift toward lower energies, with Co $2p_{3/2}$ of 1.62, 1.60 eV and Co $2p_{1/2}$ of 1.31 and 1.36 eV, respectively. The energy barrier difference between the + 2 and + 3 valence states remains stable (Fig. S12b) [47]. Except for the peaks associated with the C=O bond being accentuated as a result of the reaction of the Co-MOF with the GSH on the surface, the C 1s spectrum (Fig. S12c) is consistent with Co-MOF in terms of valence structure. No significant changes are observed in the O 1s spectrum (Fig. S12d). Compared to Co-MOF, the peaks belonging to N_2 (adsorption in the pore of Co-MOF) decrease after reaction with DA and GSH, while the changes in C–N and N–H bonds are due to the reaction of DA and GSH on their surfaces. The effect of nitrogen-containing groups on the surfaces of DA and GSH causes changes in C–N and N–H bonds (Fig. S12e). Furthermore, in Fig. S12f, it can be seen that their XRD patterns are almost identical to that before the reaction. In general, the structure of Co-MOF is still pretty stable before and after the reaction.

To evaluate the practicality of this colorimetric sensor, we also examined GSH and DA in human urine. The experimental procedure was the same as that in acetate buffer. Adding different amounts of GSH and DA to 1% human urine, it can be seen that the absorption peak at 652 nm in the UV spectrum gradually decreases with the gradual increase of GSH content in Fig. S13a and has a good linear relationship $y = -0.03528x + 0.52171$ from 0 to 12 μmol·L^{-1} detection range (Fig. S13b). Similarly, there is also a similar downward trend in the UV spectrum after adding different concentrations of DA (Fig. S13c), which also had a good linear relationship $y = -0.01111x + 0.44369$ in the detection range from 0 to 40 μmol·L^{-1} (Fig. S13d). Next, we examine its selectivity

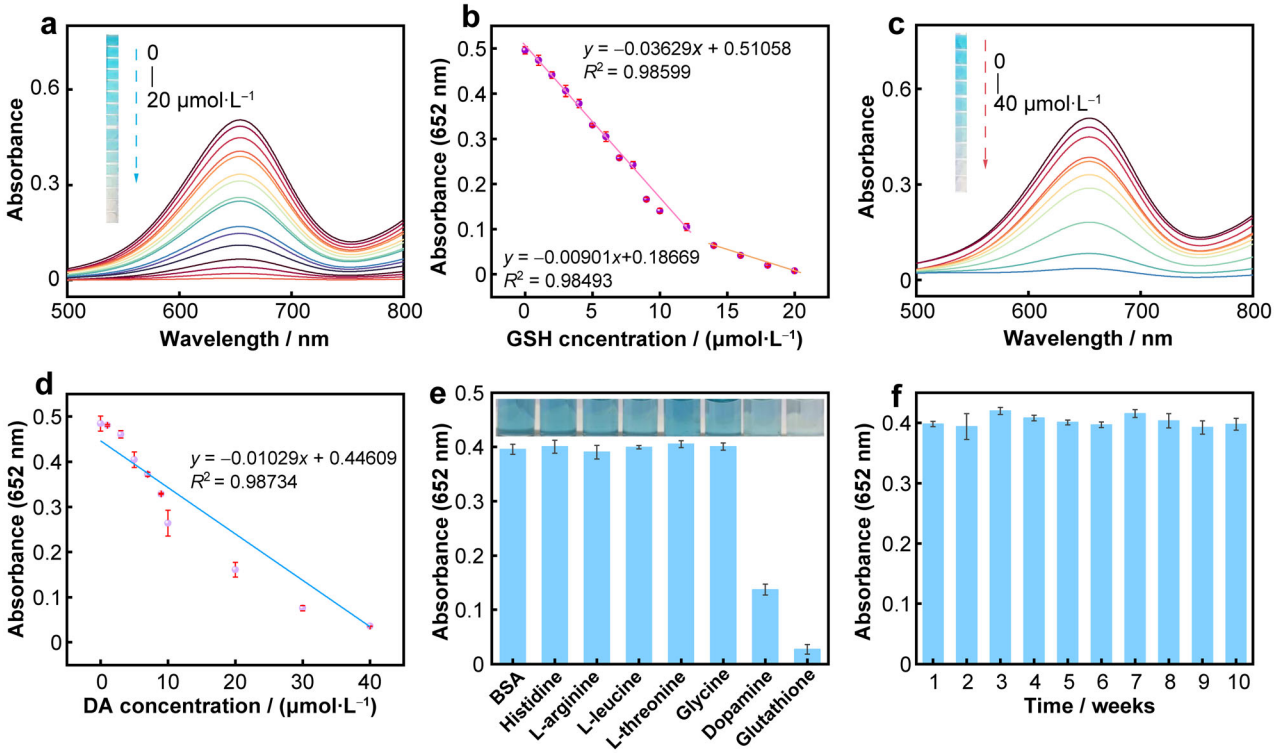

Fig. 5 **a** UV–Vis absorption spectra of oxTMB at different GSH concentrations; **b** linear relationship between absorbance at 652 nm and GSH concentrations; **c** UV–Vis absorption spectra of oxTMB at different DA concentrations; **d** a linear relationship between absorbance at 652 nm and DA concentrations; **e** specificity analysis of GSH and DA detection: difference in absorbance between GSH, DA, and other amino acids; **f** absorbance at 652 nm of oxTMB in the presence of Co-MOF at different weeks, where error bars represent standard deviation for three measurements

in real samples (Fig. S14), and it can be seen that the Co-MOF nanosheets have good selectivity for GSH and DA. Table S3 shows the results of the assay in real samples, and all data are based on three replicate measurements. It can be seen that our method has good detectability for GSH and DA. Meanwhile, the recoveries of GSH and DA range from 97.0% to 102.9% and from 98.5% to 101.2% with RSD less than 5.8% and 8.0%, respectively, indicating that the established method is feasible and reliable for the detection of GSH and DA in biological fluids.

To summarize, we have successfully constructed a 2D Co-MOF nanosheet structure, which exhibited excellent OXD-like activity and long-term stability. Based on these results, a simple, sensitive and selective colorimetric method was established for the quantitative detection of DA and GSH. The linearity between the analyte concentration and absorption ranged from 0 to 12 μmol·L^{-1} for GSH and 0 to 40 μmol·L^{-1} for DA with a detection limit of 0.24 and 0.067 μmol·L^{-1} for GSH and DA. In addition, it also has an excellent performance in the detection of real samples. This enlightening strategy not only provides a new method for the preparation of efficient MOF nanozymes but also facilitates the future development of sensitive monitoring of other biomolecules.

Acknowledgments This study was financially supported by the National Natural Science Foundation of China (Nos. 52272212 and 51802118).

Declarations

Conflict of interests The authors declare that they have no conflict of interest.

References

[1] Gao LZ, Zhuang J, Nie L, Zhang JB, Zhang Y, Gu N, Wang TH, Feng J, Yang DL, Perrett S, Yan XY. Intrinsic peroxidase-like activity of ferromagnetic nanoparticles. Nat Nanotechnol. 2007; 2(9):577. https://doi.org/10.1038/nnano.2007.260.

[2] Manea F, Houillon FB, Pasquato L, Scrimin P. Nanozymes: gold-nanoparticle-based transphosphorylation catalysts. Angew Chem Int Ed. 2004;43(45):6165. https://doi.org/10.1002/anie.200460649.

[3] Wei H, Wang EK. Nanomaterials with enzyme-like characteristics (nanozymes): next-generation artificial enzymes. Chem Soc Rev. 2013;42(14):6060. https://doi.org/10.1039/C3CS35486E.

[4] Lin YH, Ren JS, Qu XG. Catalytically active nanomaterials: a promising candidate for artificial enzymes. Acc Chem Res. 2014;47(4):1097. https://doi.org/10.1021/ar400250z.

[5] Yang RQ, Liang N, Chen XY, Wang LW, Song GX, Ji YC, Ren N, Lü YW, Zhang J, Yu X. Sn/Sn_3O_{4-x} heterostructure rich in

oxygen vacancies with enhanced visible light photocatalytic oxidation performance. Int J Min Met Mater. 2021;28(1):150. https://doi.org/10.1007/s12613-020-2131-z.
[6] Kotov NA. Inorganic nanoparticles as protein mimics. Science. 2010;330(6001):188. https://doi.org/10.1126/science.1190094.
[7] Wu JJX, Wang XY, Wang Q, Lou ZP, Li SR, Zhu YY, Qin L, Wei H. Nanomaterials with enzyme-like characteristics (nanozymes): next-generation artificial enzymes (II). Chem Soc Rev. 2019;48(4):1004. https://doi.org/10.1039/C8CS00457A.
[8] Huang YY, Ren JS, Qu XG. Nanozymes: classification, catalytic mechanisms, activity regulation, and applications. Chem Rev. 2019;119(6):4357. https://doi.org/10.1021/acs.chemrev.8b00672.
[9] Yang RQ, Song GX, Wang LW, Yang ZW, Zhang J, Zhang X, Wang S, Ding LH, Ren N, Wang AZ, Yu X. Full solar-spectrum-driven antibacterial therapy over hierarchical Sn_3O_4/PDINH with enhanced photocatalytic activity. Small. 2021;17(39):2102744. https://doi.org/10.1002/smll.202102744.
[10] Jiang B, Duan DM, Gao LZ, Zhou MJ, Fan KL, Tang Y, Xi JQ, Bi YH, Tong Z, Gao GF, Xie N, Tang AF, Nie GH, Liang MM, Yan XY. Standardized assays for determining the catalytic activity and kinetics of peroxidase-like nanozymes. Nat Protoc. 2018;13(7):1506. https://doi.org/10.1038/s41596-018-0001-1.
[11] Wang LW, Li B, You Z, Wang AZ, Chen XY, Song GX, Yang L, Chen D, Yu X, Liu J, Chen CY. Heterojunction of vertically arrayed MoS_2 nanosheet/N-doped reduced graphene oxide enabling a nanozyme for sensitive biomolecule monitoring. Anal Chem. 2021;93(32):11123. https://doi.org/10.1021/acs.analchem.1c01550.
[12] Tao Y, Ju EG, Ren JS, Qu XG. Bifunctionalized mesoporous silica-supported gold nanoparticles: intrinsic oxidase and peroxidase catalytic activities for antibacterial applications. Adv Mater. 2015;27(6):1097. https://doi.org/10.1002/adma.201405105.
[13] Wang LW, Gao FE, Wang AZ, Chen XY, Li H, Zhang X, Zheng H, Ji R, Li B, Yu X, Liu J, Gu ZJ, Chen FL, Chen CY. Defect-rich adhesive molybdenum disulfide/rGO vertical heterostructures with enhanced nanozyme activity for smart bacterial killing application. Adv Mater. 2020;32(48):2005423. https://doi.org/10.1002/adma.202005423.
[14] Luo WJ, Zhu CF, Su S, Li D, He Y, Huang Q, Fan CH. Self-catalyzed, self-limiting growth of glucose oxidase-mimicking gold nanoparticles. ACS Nano. 2010;4(12):7451. https://doi.org/10.1021/nn102592h.
[15] Tang J, Hui ZZ, Hu T, Cheng X, Guo JH, Li ZR, Yu H. A sensitive acetaminophen sensor based on Co metal-organic framework (ZIF-67) and macroporous carbon composite. Rare Met. 2022;41(1):189. https://doi.org/10.1007/s12598-021-01709-0.
[16] Wang ZJ, Li Q, Tan LL, Liu CG, Shang L. Metal-organic frameworks-mediated assembly of gold nanoclusters for sensing applications. J Anal Test. 2022;6(2):163. https://doi.org/10.1007/s41664-022-00224-0.
[17] Singh BK, Lee S, Na K. An overview on metal-related catalysts: metal oxides, nanoporous metals and supported metal nanoparticles on metal organic frameworks and zeolites. Rare Met. 2020;39(7):751. https://doi.org/10.1007/s12598-019-01205-6.
[18] Sun YJ, Jin H, Jiang XW, Gui RJ. Assembly of black phosphorus nanosheets and MOF to form functional hybrid thin-film for precise protein capture, dual-signal and intrinsic self-calibration sensing of specific cancer-derived exosomes. Anal Chem. 2020;92(3):2866. https://doi.org/10.1021/acs.analchem.9b05583.
[19] Ding LH, Yan F, Zhang YH, Liu L, Yu X, Liu H. Microflowers comprised of Cu/Cu_xO/NC nanosheets as electrocatalysts and horseradish peroxidase mimics. ACS Appl Nano Mater. 2020;3(1):617. https://doi.org/10.1021/acsanm.9b02156.
[20] Li C, Zhao DH, Long HL, Li M. Recent advances in carbonized non-noble metal–organic frameworks for electrochemical catalyst of oxygen reduction reaction. Rare Met. 2021;40(10):2657. https://doi.org/10.1007/s12598-020-01694-w.
[21] Wang JM, Shao D, Jiang LL, Li HX, Gao YJ, Rao SQ, Yang ZQ. Synthesis of rod-like NiO-Co_3O_4 composites for sensitive electrochemical detection of hydrogen peroxide. J Anal Test. 2021. https://doi.org/10.1007/s41664-021-00202-y.
[22] Farha OK, Hupp JT. Rational design, synthesis, purification, and activation of metal-organic framework materials. Acc Chem Res. 2010;43(8):1166. https://doi.org/10.1021/ar1000617.
[23] Natalio F, André R, Hartog AF, Stoll B, Jochum KP, Wever R, Tremel W. Vanadium pentoxide nanoparticles mimic vanadium haloperoxidases and thwart biofilm formation. Nat Nanotechnol. 2012;7(8):530. https://doi.org/10.1038/nnano.2012.91.
[24] Meek ST, Greathouse JA, Allendorf MD. Metal-organic frameworks: a rapidly growing class of versatile nanoporous materials. Adv Mater. 2011;23(2):249. https://doi.org/10.1002/adma.201002854.
[25] Li MH, Chen JX, Wu WW, Fang YX, Dong SJ. Oxidase-like MOF-818 nanozyme with high specificity for catalysis of catechol oxidation. J Am Chem Soc. 2020;142(36):15569. https://doi.org/10.1021/jacs.0c07273.
[26] Wang CH, Tang GE, Tan HJ. Colorimetric determination of mercury(II) via the inhibition by ssDNA of the oxidase-like activity of a mixed valence state cerium-based metal-organic framework. Microchim Acta. 2018;185(10):475. https://doi.org/10.1007/s00604-018-3011-3.
[27] Jin T, Li YL, Jing WJ, Li YC, Fan LZ, Li XH. Cobalt-based metal organic frameworks: a highly active oxidase-mimicking nanozyme for fluorescence “turn-on” assays of biothiol. Chem Commun. 2020;56(4):659. https://doi.org/10.1039/C9CC06840F.
[28] Zheng LX, Song JL, Ye XY, Wang YZ, Shi XW, Zheng HJ. Construction of self-supported hierarchical NiCo-S nanosheet arrays for supercapacitors with ultrahigh specific capacitance. Nanoscale. 2020;12(25):13811. https://doi.org/10.1039/D0NR02976A.
[29] Luo J, Dai YX, Xu XM, Liu YZ, Yang SG, He H, Sun C, Xian QM. Green and efficient synthesis of Co-MOF-based/g-C_3N_4 composite catalysts to activate peroxymonosulfate for degradation of the antidepressant venlafaxine. J Colloid Interface Sci. 2022;610:280. https://doi.org/10.1016/j.jcis.2021.11.162.
[30] Strauss I, Mundstock A, Hinrichs D, Himstedt R, Knebel A, Reinhardt C, Dorfs D, Caro J. The interaction of guest molecules with Co-MOF-74: a Vis/NIR and raman approach. Angew Chem Int Ed. 2018;57(25):7434. https://doi.org/10.1002/anie.201801966.
[31] Li JL, Jiao L, Xu WQ, Yan HY, Chen GJ, Wu Y, Hu LY, Gu WL. Cobalt oxyhydroxide nanosheets integrating with metal indicator enable sensitive detection of glutathione. Sens Actuat B Chem. 2021;329:129247. https://doi.org/10.1016/j.snb.2020.129247.
[32] Zhao J, Dong WF, Zhang XD, Chai HX, Huang YM. FeNPs@Co_3O_4 hollow nanocages hybrids as effective peroxidase mimics for glucose biosensing. Sens Actuat B Chem. 2018;263:575. https://doi.org/10.1016/j.snb.2018.02.151.
[33] Chen QM, Zhang XD, Li SQ, Tan JK, Xu CJ, Huang YM. MOF-derived Co_3O_4@Co-Fe oxide double-shelled nanocages as multi-functional specific peroxidase-like nanozyme catalysts for chemo/biosensing and dye degradation. Chem Eng J. 2020;395:125130. https://doi.org/10.1016/j.cej.2020.125130.

[34] Shen XM, Liu WQ, Gao XJ, Lu ZH, Wu XC, Gao XF. Mechanisms of oxidase and superoxide dismutation-like activities of gold, silver, platinum, and palladium, and their alloys: a general way to the activation of molecular oxygen. J Am Chem Soc. 2015;137(50):15882. https://doi.org/10.1021/jacs.5b10346.
[35] Kim Y, Kim MG. HPLC-UV method for the simultaneous determinations of ascorbic acid and dehydroascorbic acid in human plasma. Transl Clin Pharmacol. 2016;24(1):37. https://doi.org/10.12793/tcp.2016.24.1.37.
[36] Vatansever F, de Melo WCMA, Avci P, Vecchio D, Sadasivam M, Gupta A, Chandran R, Karimi M, Parizotto NA, Yin R, Tegos GP, Hamblin MR. Antimicrobial strategies centered around reactive oxygen species-bactericidal antibiotics, photodynamic therapy, and beyon. FEMS Microbiol Rev. 2013;37(6):955. https://doi.org/10.1111/1574-6976.12026.
[37] Long R, Huang H, Li YP, Song L, Xiong YJ. Palladium-based nanomaterials: a platform to produce reactive oxygen species for catalyzing oxidation reactions. Adv Mater. 2015;27(44):7025. https://doi.org/10.1002/adma.201502068.
[38] Wang ZZ, Zhang Y, Ju EG, Liu Z, Cao FF, Chen ZW, Ren JS, Qu XG. Biomimetic nanoflowers by self-assembly of nanozymes to induce intracellular oxidative damage against hypoxic tumors. Nat Commun. 2018;9(1):3334. https://doi.org/10.1038/s41467-018-05798-x.
[39] Song LF, Zhu Y, Yang ZZ, Wang C, Lu XF. Oxidase-mimicking activity of perovskite $LaMnO_{3+\delta}$ nanofibers and their application for colorimetric sensing. J Mater Chem B. 2018;6(37):5931. https://doi.org/10.1039/C8TB01706A.
[40] Qin L, Wang X, Liu YF, Wei H. 2D-metal-organic-framework-nanozyme sensor arrays for probing phosphates and their enzymatic hydrolysis. Anal Chem. 2018;90(16):9983. https://doi.org/10.1021/acs.analchem.8b02428.
[41] Herzenberg LA, De Rosa SC, Dubs JG, Roederer M, Anderson MT, Ela Stephen W, Deresinski Stanley C, Herzenberg LA. Glutathione deficiency is associated with impaired survival in HIV disease. PNAS. 1997;94(5):1967. https://doi.org/10.1073/pnas.94.5.1967.
[42] Townsend DM, Tew KD, Tapiero H. The importance of glutathione in human disease. Biomed Pharmacother. 2003;57(3):145. https://doi.org/10.1016/S0753-3322(03)00043-X.
[43] Smeyne M, Smeyne RJ. Glutathione metabolism and Parkinson's disease. Free Radic Biol Med. 2013;62:13. https://doi.org/10.1016/j.freeradbiomed.2013.05.001.
[44] Darbin O. The aging striatal dopamine function. Parkinsonism Relat Disord. 2012;18(5):426. https://doi.org/10.1016/j.parkreldis.2011.11.025.
[45] Gorwood P, Le Strat Y, Ramoz N, Dubertret C, Moalic JM, Simonneau M. Genetics of dopamine receptors and drug addiction. Hum Genet. 2012;131(6):803. https://doi.org/10.1007/s00439-012-1145-7.
[46] Grace AA. Dopamine system dysregulation by the hippocampus: implications for the pathophysiology and treatment of schizophrenia. Neuropharmacology. 2012;62(3):1342. https://doi.org/10.1016/j.neuropharm.2011.05.011.
[47] Zhang XD, Lu YW, Chen QM, Huang YM. A tunable bifunctional hollow Co_3O_4/MO_3 (M = Mo, W) mixed-metal oxide nanozyme for sensing H_2O_2 and screening acetylcholinesterase activity and its inhibitor. J Mater Chem B. 2020;8(30):6459. https://doi.org/10.1039/D0TB01337D.